Post-failure deformation mode switching in volcanic rock

Jamie Farquharson, Michael Heap, Lucille Carbillet, Patrick Baud

To cite this version:

Jamie Farquharson, Michael Heap, Lucille Carbillet, Patrick Baud. Post-failure deformation mode switching in volcanic rock. Royal Society Open Science, 2024, 11 (8), 10.1098/rsos.240792 . hal-04744021

HAL Id: hal-04744021
https://hal.science/hal-04744021v1

ROYAL SOCIETY
OPEN SCIENCE

royalsocietypublishing.org/journal/rsos

Research

Post-failure deformation mode switching in volcanic rock

Jamie I. Farquharson[1,2], Michael J. Heap[3,4], Lucille Carbillet[5] and Patrick Baud[3]

[1]Institute for Research Administration, and [2]Research Institute for Natural Hazards and Disaster Recovery, Niigata University, Ikarashi 2-8050, Nishi-ku, Niigata 950-2181, Japan
[3]Université de Strasbourg, CNRS, Institut Terre et Environnement de Strasbourg, UMR 7063, 5 rue Descartes, Strasbourg F-67084, France
[4]Institut Universitaire de France (IUF), Paris, France
[5]Laboratory of Experimental Rock Mechanics, Ecole Polytechnique Fédérale de Lausanne, Lausanne, Switzerland

JIF, 0000-0003-4933-2607

Cite this article: Farquharson JI, Heap MJ, Carbillet L, Baud P. 2024 Post-failure deformation mode switching in volcanic rock. *R. Soc. Open Sci.* **11**: 240792.
https://doi.org/10.1098/rsos.240792

Received: 14 May 2024
Accepted: 5 July 2024

Subject Category:
Earth and environmental science

Subject Areas:
volcanology, geology, geophysics

Keywords:
compaction, dilatancy, brittle-ductile transition, andesite, rock deformation, permeability

Author for correspondence:
Jamie I. Farquharson
e-mails: jifarq89@googlemail.com; jfarquharson@gs.niigata-u.ac.jp

Beyond a threshold applied compressive stress, porous rocks typically undergo either dilatant or compactant inelastic deformation and the response of their physical properties to deformation mode is key to mass transport, heat transport and pressure evolution in crustal systems. Transitions in failure modes—involving switches between dilatancy and compaction—have also been observed, but to date have received little attention. Here, we perform a series of targeted mechanical deformation experiments on porous andesites, designed to elucidate complex post-failure deformation behaviour. By investigating a sample suite and effective pressure range that straddles the transition between positive and negative volumetric responses to compression, we show two post-failure critical stress states: a transition from compaction to dilation ($C^{*\prime}$), and a transition from dilation to compaction, which we term $C^{\prime *}$. We demonstrate that multiple switches in deformation mode can be driven by stress application under conditions relevant to the shallow crust. While the effect on fluid flow properties of compaction-to-dilation switching may be masked by a net reduction in sample porosity, samples that underwent dilatant-to-compactant failure mode switching exhibited an increase in permeability of approximately two orders of magnitude, despite only slight net volumetric change. Such a substantial permeability enhancement underscores the importance of post-failure deformation in influencing solute and heat transfer in the crust, and the generation of supra-hydrostatic fluid pressures in volcanic environments.

Electronic supplementary material is available online at https://doi.org/10.6084/m9.figshare.c.7414276.

THE ROYAL SOCIETY
PUBLISHING

1. Introduction

Permeability is a critical parameter in the crust because it is a process-limiting property [1,2]. For example, permeability determines the capacity of a geologic system for mass and heat transfer [3], and governs the generation of supra-hydrostatic fluid pressures [4], which is of fundamental importance to volcanic activity and associated hazards [5–7]. Permeability can vary by multiple orders of magnitude in volcanic systems, in particular as a function of porosity [8–13]. Porosity and the connectivity of porosity can evolve in both space and time; models and experiments demonstrate that this can lead to a corresponding change in permeability [14–19].

The mechanical response of subsolidus volcanic rock to applied differential stress may be dilatant (porosity-increasing, characterized by formation of localized fracturing) or compactant (porosity-decreasing, characterized by cataclasis and pore collapse). Whether or not a rock is dilatant or compactant depends on several parameters, including the pre-existing pore structure of the rock and the chemical, thermal and mechanical conditions under which it is deformed [20,21]. Generally, at low confining pressures—which we may broadly equate to shallow crustal depths—and low initial porosity ϕ_0, we may expect shear localization to occur in volcanic rock, whereas ductile (compactant) behaviour is facilitated by relatively higher confining pressures (i.e. deeper environments) and higher ϕ_0 [17,22–26]. Whether parts of a volcanic edifice—subject to a broad range of local and regional stresses—undergo dilation or compaction as a result of *in situ* stresses is critical in terms of the structural stability of a volcano [27,28] and its capacity for outgassing volatiles [6], in turn linked to overpressure generation and attendant volcanic hazards. Drilling data reveal that the internal structure of the upper conduit architecture of silicic to intermediate volcanoes is often characterized by intense fracturing and sheared margins in the upper few kilometres, noted for example at Unzendake, Japan [29] and Nigorikawa Caldera, Japan [30]. Such a diversity of textures may well be indicative of multiple overprinting of brittle and ductile deformation mechanisms, but such processes have received little attention in laboratory-based studies.

The influence of deformation—particularly post-failure deformation—on the fluid transport properties of volcanic materials is not well studied. Fortin *et al*. [31] showed experimentally that the permeability of a low-porosity basalt was enhanced following macroscopic shear fracture, but also revealed that the direction and magnitude of permeability evolution was not constant during deformation. Farquharson *et al*. [32] performed triaxial deformation experiments on suites of variably porous volcanic rocks, demonstrating progressive porosity and permeability increase relative to the initial conditions following post-failure strain accumulation in the brittle regime. On the other hand, Heap *et al*. [16] report a net decrease in permeability for samples of trachyandesite undergoing continued deformation following brittle failure. In the ductile regime, post-failure strain accumulation in volcanic rocks has been associated with a decrease in porosity and permeability in andesite [16,17,33]. Alam *et al*. [34] investigated permeability evolution of Shikotsu welded tuff, finding that permeability decreased monotonically with triaxial compression (both in dilation and compaction) and that the rate of permeability decrease was tied to the effective pressure under which deformation was performed. More complex behaviour was observed by Farquharson *et al*. [35]: at axial strain (ϵ) less than 0.05, andesite samples exhibited an increase in permeability by approximately an order of magnitude relative to their initial state, despite a decrease in porosity; beyond $\epsilon = 0.05$, both porosity and permeability tended to decrease with increased strain accumulation.

Previous studies that have investigated the post-failure evolution of permeability of volcanic materials have primarily done so under conditions whereat the post-failure porosity evolution has been monotonic (i.e. brittle failure followed by progressively dilatant deformation, or progressive inelastic compaction during ductile deformation). Typically, brittle triaxial experiments are arrested shortly after the initial stress drop associated with macroscopic fracturing, while ductile experiments are stopped after a few per cent of sample shortening (strain accumulation). However, under certain triaxial conditions and sufficient inelastic strain accumulation, it has been observed that deformation can result in non-monotonic porosity evolution, manifest as a switch from compaction to dilation. This has been observed frequently in limestones [20,36], but also sandstones [20,37] and andesite [17,35]. Such transitional behaviours remain understudied in volcanic rocks, despite the fact that the conditions under which they are achieved are relevant to shallow volcanic environments. To address this knowledge gap, we perform a series of targeted mechanical deformation experiments on volcanic rocks of intermediate porosity (approx. 0.14–0.21), designed to showcase post-failure transitional behaviour and quantify the corresponding evolution of fluid transport properties.

2. Material and methods

The primary material used throughout this study is an andesitic lava collected from Mount Ruapehu in the Taupō Volcanic Zone (Aotearoa New Zealand). A hand sample was collected on the northern flank of the volcano [38], part of the Whakapapa Formation—the youngest unit of the Ruapehu edifice [39]. The site is culturally and ecologically protected: sampling was confined to a small block, leaving no trace of sampling, in line with sample permit guidelines and cultural consideration. From the initial block, a suite (13) of 20 mm diameter cores were prepared and precision-ground to a length of 40 ± 1 mm so that their end faces were flat and parallel. After drying the samples under vacuum, porosity was measured by helium pycnometry, and gas permeability was measured using the set-up described in Farquharson *et al*. [40]. This andesite (block R10) was selected primarily due to its intermediate porosity (mean $\phi_0 \sim 0.16$), which falls between the end-member sample sets used previously to investigate exclusively dilatant [41] or exclusively compactant [35] post-failure processes. More importantly, the sample porosities in this study fall within the range of modal porosities of compiled field data [10,42,43], suggesting that the sample behaviours are relevant to a significant proportion of the edifice, by volume. An additional single experiment was performed on a sample of La Lumbre andesite (LLB) from Volcán de Colima (Mexico), from the same suite as described in Farquharson *et al*. [35]. This sample was also characterized as described above. Ruapehu and Volcán de Colima have many characteristics in common with each other (and more broadly with many convergent margin volcanoes), including their overall geomorphology and their histories of collapse events, cyclic eruptive behaviour and periods of dome effusion. Moreover, recent eruptive products have been compositionally similar: the dome-forming lavas from Volcán de Colima (58–61 wt% SiO_2 [44]) fall within the compositional range of the Whakapapa Formation unit (57–66 wt% [39]). The lavas from both systems tend to be microstructurally complex [38,44]: highly crystalline, porous and pervasively microcracked.

Core samples were soldered into copper foil and saturated under vacuum with deionized water, then deformed in the triaxial rig at the Strasbourg Institute of Earth and Environment in France (a schematic of the device and description of the method are given in Farquharson *et al*. [35]). During deformation, we assume an effective pressure $\langle p \rangle$ [45,46] such that $\langle p \rangle = \sigma_3 - \alpha p$, where σ_3 is the confining pressure (p_c), p is the interstitial pore fluid pressure and α is the Biot–Willis coefficient [47,48]. By performing triaxial deformation experiments with nominally the same $\langle p \rangle$ but different p, Farquharson *et al*. [49] show that for a Volcán de Colima andesite, α can be assumed to equal 1. Given the similarities described above, we further assume that this is the case for all andesites in this study. Values of effective pressure $\langle p \rangle$ of 10, 30, 50 or 70 MPa were imposed on the samples (with a pore pressure p of 10 MPa). To deform samples, a differential stress ($\sigma_1 - \sigma_3$) was applied in the direction of the sample axis by advancing a servo-controlled axial piston at a constant strain rate of 10^{-5} s^{-1}, sufficiently slow to ensure that the sample remains fluid-saturated and drained throughout the experiment [50]. Confining and pore pressures are also servo-controlled; accordingly, variations in sample pore volume during deformation are recorded by the pore fluid actuator, as it compensates for pore fluid pressure changes [51]. Normalized to the sample volume, this response corresponds to porosity change $\delta\phi$, which for porous rock can be considered approximately equivalent to the volumetric strain (see [52]). Deformation was allowed to continue post-failure to a target axial strain. The target value varied between experiments, from $\epsilon = 0.02$ up to a maximum of $\epsilon = 0.25$ (a 25% shortening of the sample). Because the axial piston has a finite stroke length, large amounts of strain were achieved by periodically isolating the sample within the pressure vessel and recharging the loading ram before continued deformation. In practice, this involves closing the valve that connects the pressure vessel to the axial piston system (i.e. valve 3 in the schematic of [35]) and retracting the piston towards its initial position. During this time, the piston head is not under servo-control, and thus some drift is anticipated and corrected for manually: this can manifest as transient minor stress reductions in the raw data, which can be accounted for during data processing. After deformation, samples were unloaded and their permeability remeasured (see [35]). In the following, we adopt the convention that compressive stress and compactant strain are positive. All experiments were carried out at room temperature. Select deformed and undeformed samples were imaged using a scanning electron microscope (SEM). SEM analysis of the Ruapehu andesite reveals a porphyritic juvenile andesite with abundant tabular plagioclase phenocrysts set in a dense glassy microlitic matrix. The main pore shape families are (i) approximately circular, with characteristic length-scales of the order of 100 μm, and (ii) highly amœboid and frequently elongate pores with diameter of the order of 1000 μm.

However, these end-members fall on a spectrum and there is no clear threshold between the two. Pores are variably interconnected by microcracks.

3. Results and discussion

3.1. Influence of effective pressure and porosity on failure and deformation

Figure 1 shows representative deformation results from samples deformed under different effective pressures $\langle p \rangle$. Figure 1*a* plots differential stress $(\sigma_1 - \sigma_3)$ as a function of axial strain. For samples deformed at $\langle p \rangle$ = 10, 30 and 50 MPa, deformation is characterized by a brief concave-up signal (signifying elastic crack closure), followed by linearly increasing $(\sigma_1 - \sigma_3)/\epsilon$. After rolling over to a peak value in $\sigma_1 - \sigma_3$, we observe a stress drop (from approx. 40 to over 100 MPa) followed by quasi-constant stress with additional strain accumulation. The peak stress and stress drop are associated with the generation of a shear band: visual inspection of the failed samples reveals localized failure running subparallel to the sample axis (10 MPa) or inclined to the axis (30 and 50 MPa). It is probable that post-failure, strain is accommodated by sliding on the resultant macroscopic fracture. Under effective pressure of 70 MPa, the initial part of the curve follows the same trend. However, there is no marked drop in stress, and the sample undergoes compactant (ductile) yield rather than brittle failure. In this case, no macroscopic fracture was observed in the failed sample. We note that previous studies [17,22,23,35] have highlighted compaction localization features in porous volcanic rocks: bands or zones of collapsed pores tending sub-perpendicular to the maximum principle stress σ_1. Such localization is typically accompanied by transient, post-yield stress drops of a few MPa; in this study, we observe such stress drops for some but not all experiments in the ductile field, suggesting that compaction is manifest both in a distributed manner (diffuse microcracking and distributed pore collapse) and occasionally in a localized manner (a contiguous plane of collapsed pores).

In figure 1*b*, we show porosity change $\delta\phi$ as a function of strain ϵ for the same experiments shown in figure 1*a*. For effective pressure $\langle p \rangle = 10$ MPa, we observe an initial decrease in porosity (compaction associated with elastic crack closure), a (pre-failure) switch from compaction to dilation whereat new cracking exceeds the rate of compaction, followed by a relatively constant value of porosity change with strain. The volumetric deformation curves (figure 1*b*) confirm that the deformation behaviour of samples deformed at $\langle p \rangle > 10$ MPa is net compactant: the deformed samples are always less porous than at the start of the experiment. However, whereas at $\langle p \rangle$ = 70 MPa (the ductile experiment), $\delta\phi$ decreases monotonically with strain ϵ, this is not the case for the intermediate effective pressures (30 and 50 MPa). This is visualized in figure 1*c*, where we show the effective mean stress $\langle \bar{p} \rangle$ (a function of all stresses acting on the sample: $[\sigma_1 + 2\sigma_3]/3 - p$) against $\delta\phi$. In cases where the signal deviates leftwards from this curve—a stress threshold called C', which represents the onset of dilatant microcracking—we can define eventual failure in the brittle regime (demarcated by the stress, strain coordinates corresponding to the maximum differential stress σ_p, figure 1*a*). The corresponding macroscopic 'failure' in the ductile field is represented by a critical stress point termed C^*, which is the onset of shear-enhanced compaction. Graphically, this is the point at which the stress–strain curve deviates to the right of the hydrostatic signal (e.g. figure 1*c*). The volumetric response of the samples during deformation is further visualized in figure 1*d*, where we show the sign of the porosity change slope (figure 1*b*): decreasing or increasing porosity is denoted by – or +, respectively, and the shading indicates whether the sample is net compactant (i.e. whether it has a lower porosity than at the start of the experiment ϕ_0 at any given point during deformation).

At $\langle p \rangle$ = 10 MPa, the sample is entirely dilatant. The failure of the sample, described by σ_p, is a function of growth and coalescence of microcracks into a failure plane (a macroscopic fracture). At $\langle p \rangle$ = 70 MPa, the sample is entirely compactant and porosity continues to decrease as the sample is deformed beyond C^* (figure 1*c*,*d*). At $\langle p \rangle$ = 30 and $\langle p \rangle$ = 50 MPa, both samples exhibit an initial dilatant period (deviations to the left on figure 1*c*) leading to a peak stress: failure in the brittle regime. However, unlike the experiment performed at $\langle p \rangle$ = 10 MPa, which continued to dilate, continued post-failure strain accumulation at $\langle p \rangle$ = 30 and $\langle p \rangle$ = 50 MPa results in a transition from dilatant to compactant behaviour. As evident in figure 1*b–d*, these samples are net compactant despite having failed in the brittle field, and are characterized by C' rather than C^*. This transitional behaviour will be discussed further in §3.3. Deformation conditions and results are given in table 1.

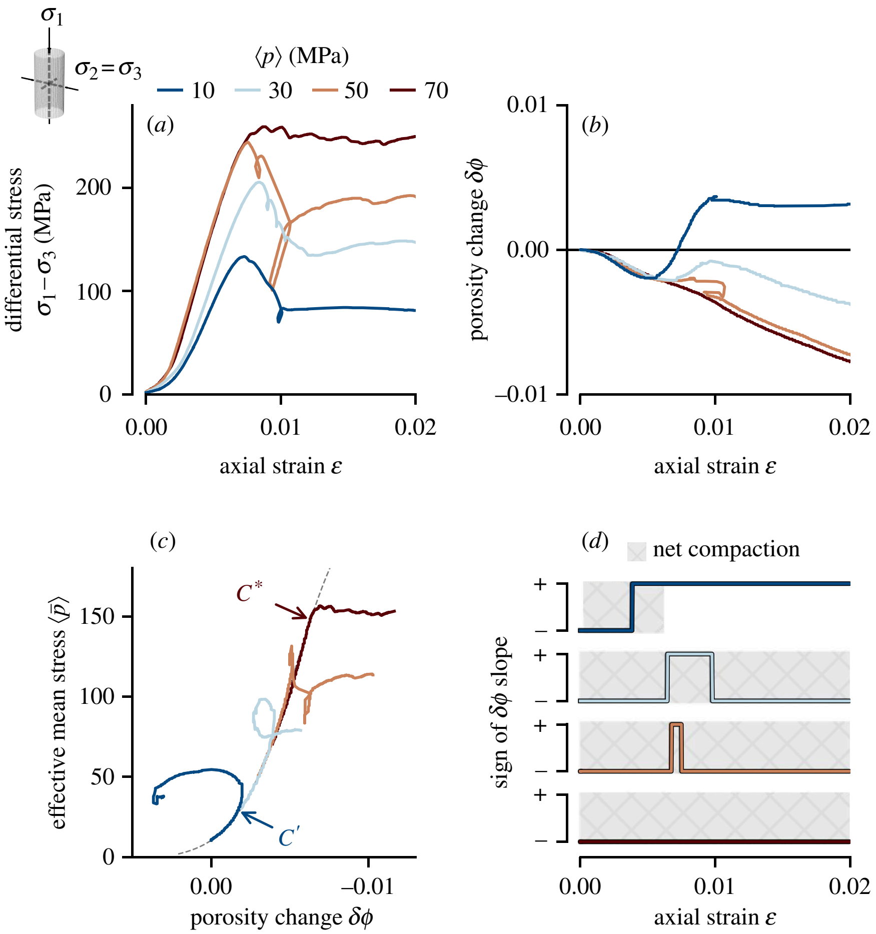

Figure 1. (*a*) Differential stress versus axial strain for andesite samples (R10–7, −15, −8 and −16) deformed at $\langle p \rangle$ = 10, 30, 50 and 70 MPa, respectively (indicated by colour). (*b*) The same samples as (*a*), showing porosity change as a function of axial strain. (*c*) Effective mean stress as a function of porosity change. The data have been offset from the *y*-axis to align with the assumed hydrostatic signal (dashed line). (*d*) The sign (positive or negative) of the porosity change slope, as shown in (*b*). Shaded area indicates periods of net compaction.

From the inelastic components of axial strain ϵ_i and porosity change $\delta\phi_i$, we can determine an inelastic compaction factor $\delta\phi_i\epsilon_i^{-1}$ [53,54]. This parameter quantifies the amount of change of sample porosity for additional increments of inelastic strain. In figure 2*a*, we plot this parameter—calculated from these experiments as well as compiled data on volcanic rocks from [17,32,35]—against the initial sample porosity ϕ_0. Some of the volcanic systems represented in the compilation are good analogues for each other (notably Ruapehu and Colima). They also comprise particularly strong analogues for many other active andesitic stratovolcanoes—including Mount Rainier (USA), Ulawun (Papua New Guinea), Llaima (Chile), Ijen (Indonesia) and Galeras (Colombia)—when their eruptive histories are considered alongside geological and geochemical characteristics [55,56]. More importantly in the context of this study, however, is the fact that these samples have been deformed using the same experimental protocol, on the same apparatus and have received the same data treatment. While variability exists within each sample suite due in part to the different degrees of axial strain (figure 2*b*) and effective pressures associated with each test [57], the influence of initial porosity ϕ_0 is clear: at low starting porosities (< 0.1), samples tend to exhibit $\delta\phi_i\epsilon_i^{-1} > 0$ whereas at higher starting porosities (> 0.15), we observe $\delta\phi_i\epsilon_i^{-1} < 0$. This is as expected: porosity is a key parameter influencing whether a rock will compact or dilate in response to applied stress [20]. Similarly, figure 2*b* shows that a tendency towards zero exists with increasing inelastic strain accumulation, irrespective of whether the inelastic compaction factor is initially positive or negative. A key feature of our experimental design is that our new data encompass the transition between $\delta\phi_i\epsilon_i^{-1} > 0$ and $\delta\phi_i\epsilon_i^{-1} < 0$. For R10 andesite (circles in figure 2*a*) samples deformed at $\langle p \rangle = 10$ MPa, we observe $\delta\phi_i\epsilon_i^{-1} > 0$, meaning that for additional increments of

Table 1. Deformation conditions and results.

sample	effective pressure (MPa)	pore pressure (MPa)	peak stress σ_p (MPa)	C^* (MPa)	$C^{*\prime}$	$C^{\prime *}$
R10–3	10	10	145.99		╳	╳
R10–4	50	10	261.8		╳	○
R10–5	50	10	279.53		╳	✓
R10–6	50	10	210.22		╳	○
R10–7	10	10	143.07		╳	╳
R10–9	50	10	267.06		╳	✓
R10–10	10	10	142.13		╳	╳
R10–11	10	10	133.3		╳	╳
R10–12	50	10	243.9		✓	○
R10–13	10	10	130.8		✓	✓
R10–15	30	10	205.39		╳	✓
R10–16	70	10		214.3	╳	╳
R10–17	70	10		254.94	╳	╳
LLB-2	30	10		54.87	✓	╳

✓critical stress state observed; ╳ critical stress state not observed; ○ intermediate stress behaviour.

inelastic axial strain, sample porosity increases. For R10 samples deformed at $\langle p \rangle \geq 30$ MPa, the inelastic compaction factor $\delta\phi_i\epsilon_i^{-1} < 0$ (figure 2*a*), meaning that for additional increments of inelastic axial strain, sample porosity decreases.

3.2. Post-failure transition from compaction to dilation

Porosity is a first-order parameter dictating deformation behaviour of porous rock [20], including porous volcanic rock [21]. However, as demonstrated in figure 1*b–d*, porosity is subject to change with continued strain. Theoretically, after a given amount of compaction, porosity may be reduced to a point whereat any additional deformation of a compacting material is accommodated by macroscopic fracturing (as it would be for an initially low-porosity material). The strain-dependent transition from compactant to dilatant behaviour is termed $C^{*\prime}$, and defines the maximum compaction that a given rock can withstand. This transition has been demonstrated experimentally in sedimentary [36,37,53,58,59] and volcanic [17,35] rocks. Heap *et al.* [17] observed $C^{*\prime}$ in a porous andesite deformed at $\langle p \rangle = 50$ MPa after an axial strain of 0.13, and a corresponding reduction in porosity $\delta\phi$ of approximately 0.04. Farquharson *et al.* [35] report $C^{*\prime}$ in a porous andesite deformed at $\langle p \rangle = 30$ MPa after an axial strain of 0.16, and a reduction in porosity $\delta\phi$ of approximately 0.05.

In figure 3*a*, we show porosity change as a function of effective mean stress for Ruapehu andesite R10–12. Initially, porosity decreases (the porosity change signal $\delta\phi$ moves rightward), equivalent to other compactant experiments presented here (e.g. figure 1*c*). However, after a reduction in sample porosity from 0.18 to 0.155 (porosity change of approximately 0.024), we observe dilatant deformation (the signal moves leftwards). This transition point, $C^{*\prime}$, is shown in more detail in figure 3*a* (inset) and corresponds to the point where the first derivative of the volumetric deformation signal (as a function of axial strain) switches sign from negative to positive.

In figure 3*b*, we compile prior data (andesites from Volcán de Colima: C8-8 and LLB-13) with data from two new experiments (Ruapehu andesite R10–12 and Colima andesite LLB-2), plotted as porosity reduction as a function of axial strain. The transition point from compaction to dilation is marked by a symbol for each sample. To account for experimental artefacts associated with recharging the axial loading ram, we first apply a one-dimensional Gaussian filter to the deformation signal $f(\delta\phi)$, then obtain the change-point at the global minimum (i.e. $f'(\delta\phi) = 0$). Generally, there is a correlation between the volume of porosity reduction required to achieve $C^{*\prime}$ and the associated axial strain (i.e.

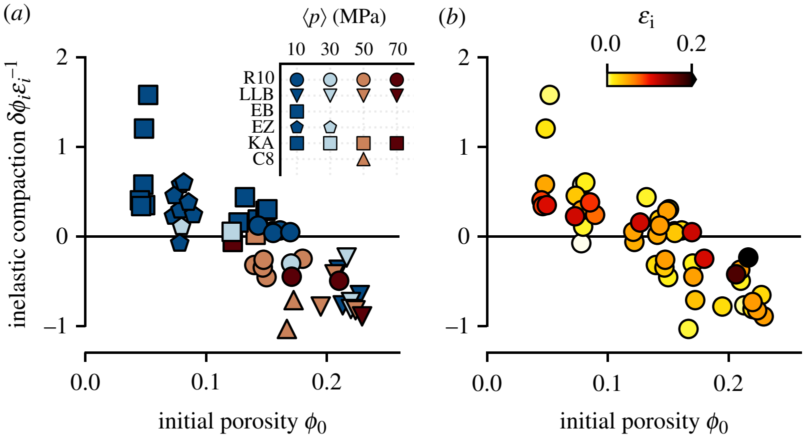

Figure 2. (*a*) Inelastic compaction factor as a function of initial porosity for samples of this study (R10) and compiled volcanic data from [32] (EB, Etna basalt, EZ, El Zarco andesite, KA, Kumamoto andesite) [17]; (C8, San Antonio andesite); and [35] (LLB, La Lumbre andesite). Colours represent $\langle p \rangle$, as in figure 1. (*b*) As (*a*), but differentiating data by inelastic strain ϵ_i.

high porosity change requires high strain (figure 3*b*). The strain at $C^{*\prime}$, labelled $\epsilon(C^{*\prime})$, is shown as a function of initial porosity ϕ_0 in figure 3*b* (inset). Our data reveal a clear dependence on the initial porosity: the axial strain required for $C^{*\prime}$ increases as ϕ_0. Although the data are too few to draw additional conclusions, there also appears to be a measurable influence of effective pressure, i.e. a greater degree of strain is required to achieve the critical stress transition at lower effective pressure for samples of similar starting porosity (figure 3*b* and inset). These observations agree with results from sedimentary rocks [36,53], despite differences in the dominant micromechanical processes. In the broader context of a volcanic system, this would suggest that compactant-to-dilatant transitional behaviour may be more prevalent in the shallow volcanic edifice than previously discussed [17] ($\langle p \rangle = 30$ MPa is approximately equivalent to 1.3 km depth beneath the summit). In §4, we further discuss the effect of this transition on fluid flow properties, with attendant implications for volcanic behaviour.

Microstructurally, we observe characteristic compactant features in Ruapehu andesite sample R10–12 (mechanical data shown in figure 2*a*). These include heavily comminuted groundmass, micrometre-scale crystal pulverization (examples circled on figure 3*c*,*d*) and other evidence of cataclastic pore collapse (arrow on figure 3*c*). These are frequently overprinted or connected in places by fractures (e.g. see arrows in figure 3*d*), as described in earlier studies on volcanic rocks [17,35].

3.3. Post-failure transition from dilation to compaction

While the compactant-to-dilatant critical stress threshold has been observed and described in prior studies (see references in §3.2), the inverse phenomenon—a transition from dilatancy to a dominantly compactive mechanism—has not been explicitly described, to the authors' knowledge. However, theoretically there should exist a stress state whereby a dilating sample undergoes an increase in porosity sufficient to encourage a compactive response to additional deformation, as posited by Meyer and Violay [60]. Herein, experiments were performed with the intention of demonstrating this transition: an example is shown in figure 4*a*. The porosity reduction curve as a function of effective mean stress is given for Ruapehu andesite R10–15 ($\phi_0 = 0.14$; $\langle p \rangle = 50$ MPa), which exhibits complex mechanical responses during prolonged deformation. The stress path is characterized by a series of critical stress states: (i) the onset of dilatancy, demarcated by C' [54]; (ii) the point at which dilation overtakes compaction, termed D' [62]; (iii) a peak stress σ_p, signifiying macroscopic failure in the brittle regime; and (iv) a post-failure transition from dilation to compaction. This latter transition is C'^{*}, and proves to be repeatable for the andesites of this study, despite inherent sample variability (figure 2*b*): this critical stress state was achieved at $\langle p \rangle = 10$, 30 and 50 MPa (table 1). Samples that have undergone C'^{*} exhibit shear fractures oriented obliquely to the maximum principal stress (see arrow in figure 4*c*). Fractures appear to have coalesced stepwise as dictated by pre-existing, irregularly shaped pores. The fractured zones are variably 100–1000 µm in width, with gouge formation [63] characterized by

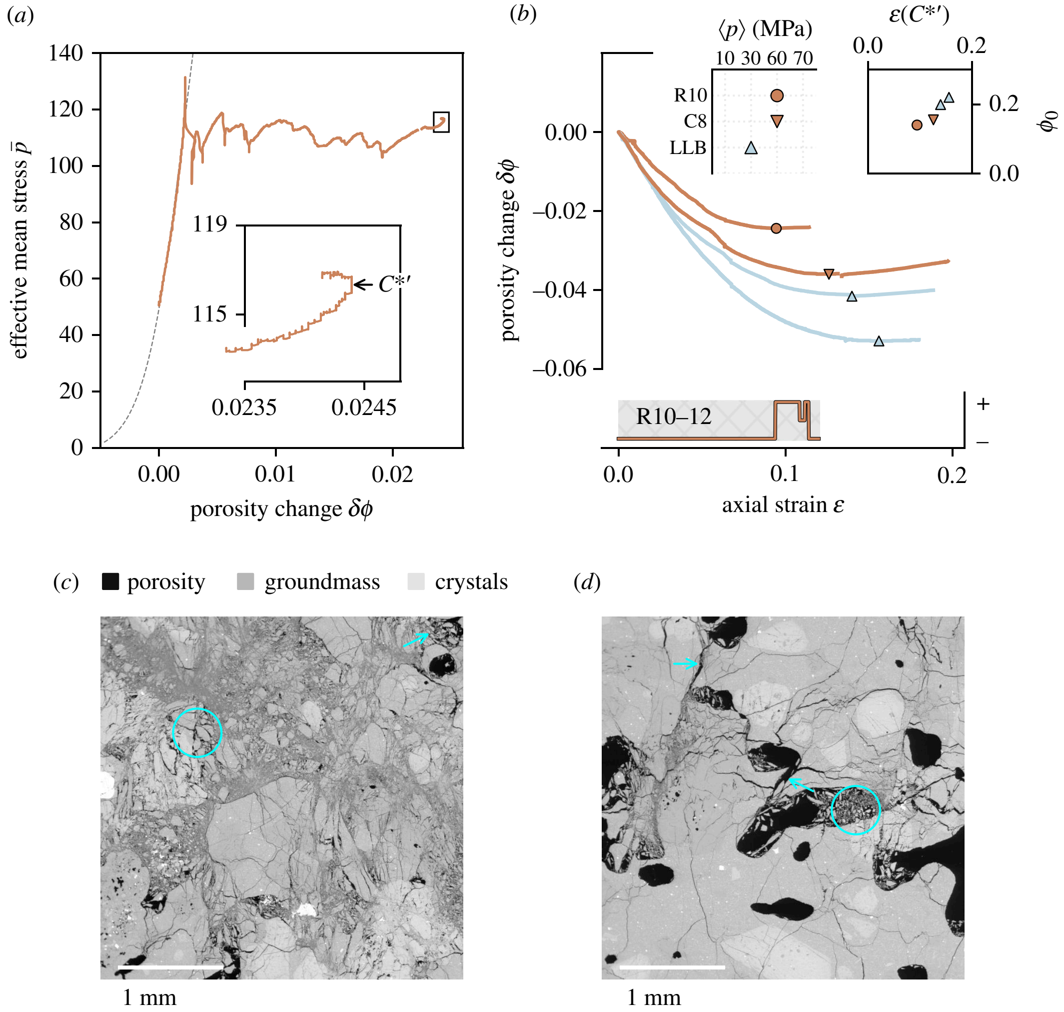

Figure 3. (*a*) Effective mean stress versus porosity change for andesite sample R10–12. Dashed line is as in figure 1*c*. Inset shows detail of critical stress state $C^{*\prime}$. (*b*) Compiled porosity change curves for andesites that have reached $C^{*\prime}$. R10–12: $\phi_0 = 0.18$, $\langle p \rangle = 50$ MPa; C8–8: $\phi_0 = 0.16$, $\langle p \rangle = 50$ MPa; LLB–13: $\phi_0 = 0.22$, $\langle p \rangle = 30$ MPa; LLB–2: $\phi_0 = 0.20$, $\langle p \rangle = 30$ MPa. Below is the sign of the porosity change slope for sample R10–12. Inset shows strain at $C^{*\prime}$ as a function of initial porosity. (*c*) SEM image of heavily comminuted groundmass (e.g. circle) and pore collapse (e.g. arrow) in R10–12, following $C^{*\prime}$. SEM images are oriented such that the maximum principal stress during deformation is oriented vertically. (*d*) Example of interconnected porosity in R10–12, whereby pores are joined by variably coalesced microcracks (highlighted by arrows). Intra-pore spalling grains, evidence of cataclastic pore collapse, are evident towards the centre of the image (cyan circle).

microfracturing and comminution, and evidence of translation and rotation of fragments (figure 4*c*). As highlighted in figure 4*d*, there is also evidence of cataclastic pore collapse (e.g. as highlighted by the cyan circles), typically inside or within a few hundred micrometres of the primary fracture zone. This is manifest as partially collapsed pores, with more intense cataclasis oriented towards the fracture plane (circled) (figure 4*d*). In light of the associated mechanical data, we interpret these microtextures as representing an initial fracture event followed by fracture zone evolution and thickening, before the onset of localized pore collapse driven by local porosity (and stress) change. Many of the textures observed in samples that have undergone $C^{*\prime}$ or $C^{\prime *}$ are similar (cf. figures 3*d* and 4*c*), although extensive fault gouge formation may be distinguishable from *in situ* cataclasis by observation of grain translation along the fault plane. We note that the primary observable difference is the macroscopic orientation of the failure localization plane(s): compaction localization (in the case of $C^{*\prime}$) is approximately perpendicular to the sample axis (figure 3*c*), whereas failure localization in the case of $C^{\prime *}$ is subparallel to the sample axis (figure 4*c*).

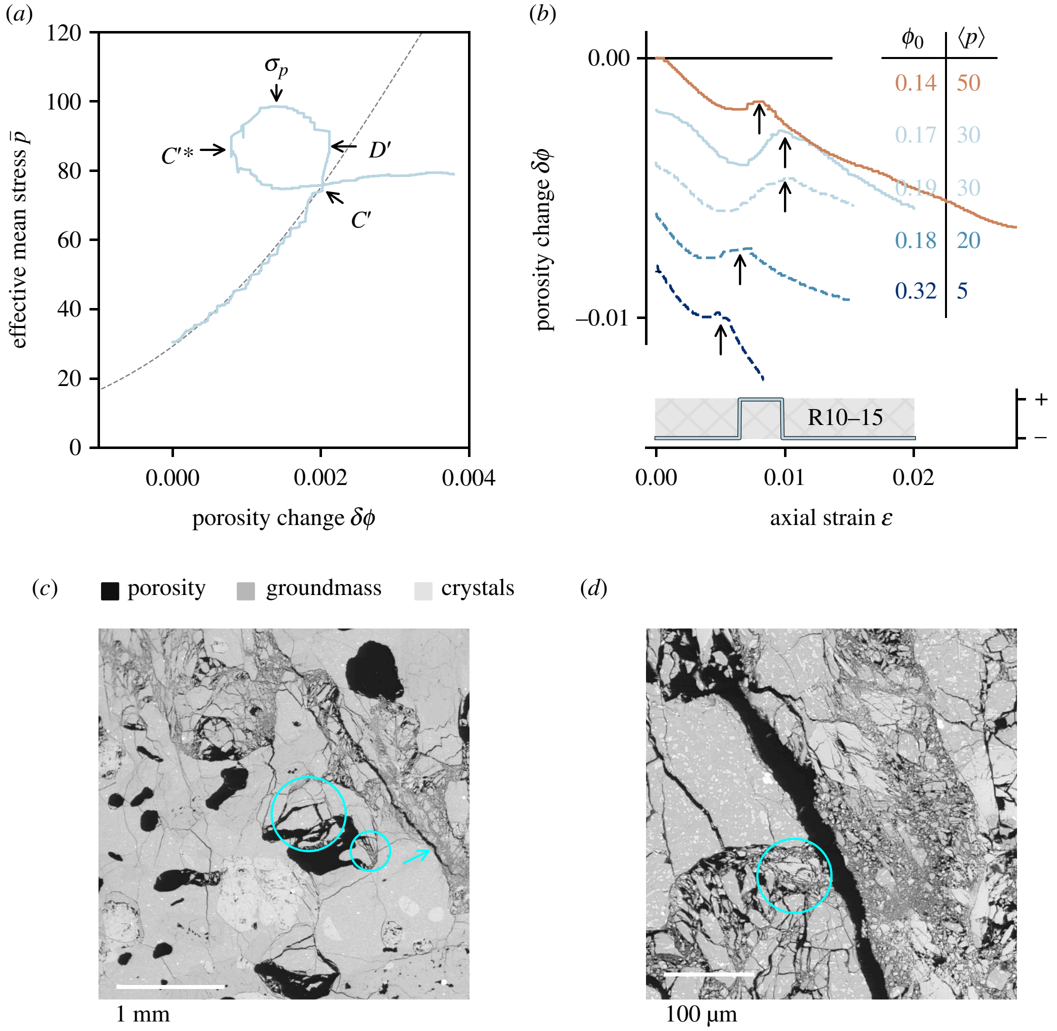

Figure 4. (*a*) Effective mean stress versus porosity change for sample R10–15, highlighting sequence of critical stress states including C'^*. (*b*) Compiled porosity change data for R10 samples and samples of Mount St Helens dacite (dashed lines) from [61]. Note that curves are vertically offset for clarity. C'^* is highlighted by an arrow in each case. Initial porosity ϕ_o and effective pressure $\langle p \rangle$ (in MPa) are indicated for each sample. Below is the sign of the porosity change slope for sample R10–15. (*c*) SEM image of sample R10–15, showing coalesced fractures (e.g. arrow) and evolved fault zone, surrounded by partially collapsed pores (circled). (*d*) Further detail of the fracture zone.

We emphasize that although this critical stress transition has not—to our knowledge—been formally described by previous authors, there exists evidence of volcanic samples achieving C'^* in some published experimental studies. The porosity change data from [61] (their figures 4*c* and 5*c*) show this phenomenon in Mount St Helens dacite; the transition is also visible in experimental data from Volvic trachyandesite ([16], their figure 3; [21], their figure 17*b*). Moreover, figure 5*a*,*f* of Carbillet *et al*. [64] seemingly documents this phenomenon in synthetic samples (sintered monodisperse glass beads, analogous to monomineralic well-sorted sandstones). Data from Heap *et al*. [61] (dashed lines) are plotted alongside data from the current study (solid lines) in figure 4*b*; the critical stress state C'^* is highlighted by the arrows. In comparable manner to the stress and porosity dependence of the 'critical state line' [17], we would anticipate the range of stresses at which the C'^* phenomenon becomes evident to scale inversely with initial sample porosity, with the implication that at high initial porosities, a post-failure switch from dilatant to compactant behaviour would occur at low effective pressure, whereas at relatively lower initial porosities, a higher effective pressure would be required to instigate this post-failure transition. In sedimentary materials, evidence for a critical state C'^* (as we define it) appears to be rare. More often, the brittle-ductile transition in sedimentary rocks is characterized by volumetrically neutral behaviour. In a graph of effective mean stress versus porosity change, this response is manifest as the curve following the hydrostat before stalling around a single point: continued deformation does not affect the bulk sample porosity (i.e. inelastic compaction factor $\delta\phi_i\epsilon_i^{-1} = 0$) [20,54,57,65,66]. The corresponding stress–strain responses in those sedimentary examples reveal that the samples do not exhibit the characteristic yield point (C^*) but continue to accumulate strain through cataclastic flow and/or the generation of compaction bands while accommodating a near-constant axial stress level. Tentatively, we attribute the differing behaviours between the volcanic rocks studied here and sedimentary rocks of prior studies to a difference in the characteristic flaw length-scale (e.g. pore radius of the lavas versus grainsize of the granular sedimentary samples), of the respective materials, but this remains a detail for future investigation. Given that volcanic deposits can be fundamentally granular (e.g. welded fall deposits), and that many volcanic systems overlie a sedimentary basement, we emphasize the importance of investigating post-failure deformation for a broad range of crustal materials and analogues.

3.4. Multiple post-failure switches in deformation mode

Continued post-failure compaction can eventually initiate dilatant deformation (§3.2, figure 3*a–b*). Likewise, we demonstrate that post-failure dilation can precede net compaction (§3.3, figure 4*a–b*). It stands to reason that there exists a range of initial sample porosities and deformation conditions such that the inelastic compaction factor $\delta\phi_i\epsilon_i^{-1}$ (figure 2*a,b*) is equal or sufficiently close to zero that small increments of strain—characterized by a slight *increase* or *decrease* in porosity—can flip the sign of $\delta\phi_i\epsilon_i^{-1}$, thereby prompting a slight *decrease* or *increase* in porosity sufficient to re-flip the sign of $\delta\phi_i\epsilon_i^{-1}$, and so on. In a final deformation experiment, we seek to capture this behaviour, selecting a sample of Ruapehu andesite (R10−13) with an initial porosity of $\phi_0 = 0.17$ and deforming it at an effective pressure $\langle p \rangle$ =10 MPa. The results are shown in figure 5, with the deformation signal of a slightly lower porosity sample (R10−11, $\phi_0 = 0.16$; $\langle p \rangle = 10$MPa) shown for reference.

The two samples follow a comparable stress evolution path until immediately prior to macroscopic failure in the brittle regime, with peak stresses (1 in figure 5*a*) of 131 MPa (sample R10−13) and 133 MPa (sample R10−11). Post-failure, both samples exhibit a phase of dilatant deformation, a function of continued fracture evolution and fault sliding [32]. After accumulating 0.009 axial strain ($\delta\phi \sim 0.0024$), sample R10−13 reaches C'^* (transition from dilatant to compactant deformation; 2 in figure 5*a,b*), as described in §3.3, whereas sample R10−11—the grey curve—does not. For sample R10−13, compaction with continued strain accumulation is manifest in figure 5*a,b* by evolution from 2 → 3. Critically, at this point, $\phi_0 + \delta\phi = \phi_0$: the sample has exactly the same porosity as at the beginning of the experiment (again, this is not true for sample R10−11). Briefly, the sign of porosity change flips as the sample undergoes *net* compaction (3 → 4), before again crossing the $\delta\phi = 0$ line and undergoing dilation. We interpret this phase (4 → 5) as reactivation of the initial macroscopic failure plane followed by fault sliding. Note that point 4 fits the definition of $C^{*\prime}$. With continued deformation, the sample undergoes a sequence of transitions from dilation–compaction–dilation–compaction–dilation, although the net porosity change of the sample remains positive. Figure 5*c* illustrates the full sequence as a function of the sign of the slope of the $\delta\phi$ signal.

In figure 6, we summarize the operative micromechanical processes discussed in this section, as informed by our experimental and microstructural data. Figure 6*a* depicts a pore (0) subject to cataclastic pore collapse as a function of ongoing deformation (1–3). Bulk sample porosity decreases relative to the initial state as the porous network is progressively occluded. Beyond a threshold stress ($C^{*\prime}$) fractures nucleate and grow (4–5), driving some increase in porosity (although not beyond the initial state). This scenario is reflective of sample R10−12, as shown in figure 3*a*. In figure 6*b*, dilatant processes are illustrated: first distributed microcracking (1), then growth and coalescence of these fractures into a localized failure plane (2), which can evolve to become a complex fracture zone (3). This progression is associated with a marked increase in porosity. Beyond the critical stress state C'^*, cataclastic pore collapse is promoted in the vicinity of the fracture zone (4), which may be reflected by a decrease in sample porosity (5). This scenario is reflective of sample R10−15, as shown in figure 4*a*. Finally, in figure 6*c*, we illustrate the proposed process leading to deformation signals such as that shown in figure 5: repeated post-failure switching between compaction-dominant and dilation-dominant deformation mechanisms. In this case, porosity fluctuates around the initial value throughout deformation, as the primary mechanism alternates between fracture generation and propagation (1, 3 and 5) and cataclastic pore collapse (2 and 4).

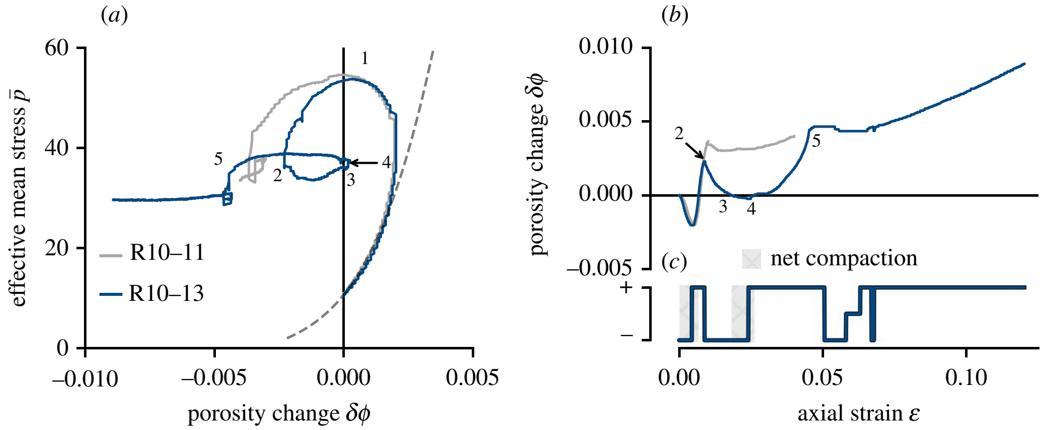

Figure 5. (*a*) Porosity change versus effective mean stress for andesite sample R10–13 (blue) and R10–11 (grey). Stress states 1–4 are described in the main text. (*b*) Porosity change curve for R10–13 and R10–11. (*c*) Sign of the porosity change curve for sample R10–13.

4. Mechanical deformation and fluid flow

Prior to deformation, we performed measurements of porosity (ϕ_0) and permeability (k_0) on all samples. The post-deformation permeability k_1 was measured under identical conditions after unloading the samples. It is worth highlighting that this procedure allows comparison between samples with different deformation histories; however, the *in situ* permeabilities will probably be lower due to the differences in confining pressure for the permeability measurements (1 MPa) and the deformation experiments (as listed in table 1). Using the porosity change signal, the post-deformation porosity can be calculated ($\phi_1 = \phi_0 + \delta\phi_i$). Figure 7 shows pre- and post-deformation porosity and permeability for the new data of this study, alongside andesites from Volcán de Colima from prior studies; these published examples are distinguished by their sampling localities, El Zarco (EZ), San Antonio (C8) and La Lumbre (LLB) and encompass a range of initial porosities and deformation behaviours. Note that LLB-13 is an andesite studied in [35], whereas LLB-2 is a sample prepared from the same block, new to this study. Plotted mechanical data are separated by effective pressure: 10 (figure 7*a*), 30 (figure 7*b*), 50 (figure 7*c*) and 70 MPa (figure 7*d*).

Results from previous data are summarized as follows. Low-ϕ_0, low-$\langle p\rangle$ deformation tends to result in large increases in permeability, and relatively little increase in porosity, e.g. EZ andesite (figure 7*a*). This is attributed to brittle failure establishing a flow path (i.e. a macroscopic fracture), which remains a highly efficient permeable pathway [54] irrespective of subsequent cataclastic mechanisms (in particular the generation of friction-induced fault gouge) [32]. High-ϕ_0, high-$\langle p\rangle$ deformation tends to result in decreases in porosity and permeability. For example, C8 andesite exhibits a concomitant decrease in both properties (figure 7*c*). Compaction in this sample is manifest as distributed cracking and pore collapse interspersed with localized planes or layers of collapsed pores (i.e. compaction bands) oriented sub-perpendicular to the direction of fluid flow [17]. Higher porosity andesites (LLB, ϕ_0~0.22) exhibit a reduction in porosity under all investigated conditions ([35]; figure 7*a–d*), but permeability change is inconsistent, exhibiting either an increase or decrease typically of less than one order of magnitude. Counter-intuitively, low amounts of compaction may increase permeability in volcanic rock as microcracks connect otherwise isolated porosity [35], a phenomenon that can be overprinted at high strain by global reduction in sample porosity. Moreover, compaction localization may not always constitute an effective barrier to fluid flow due to their tortuous and non-contiguous form [17].

At effective pressure $\langle p\rangle = 50$ and 70 MPa, the R10 andesite samples of this study agree with previous data (cf. LLB andesite, figure 7*c,d*), and emphasize the fact that permeability may increase following compaction. As highlighted by Heap *et al.* [17], the tortuous and non-contiguous geometries of compaction bands—a function of the complex pre-existing pore geometries and variable crystallinity—drive only moderate porosity reduction (0.04–0.08 reduction within the compaction bands) compared with similar features in sandstones (approx. 0.15% [67]). This observation is in line with other studies identifying compaction bands in volcanic rocks [16,17,22,23]. Thus, at higher $\langle p\rangle$, the effect of deformation is strongly dependent on both the angle and relative permeability of compaction

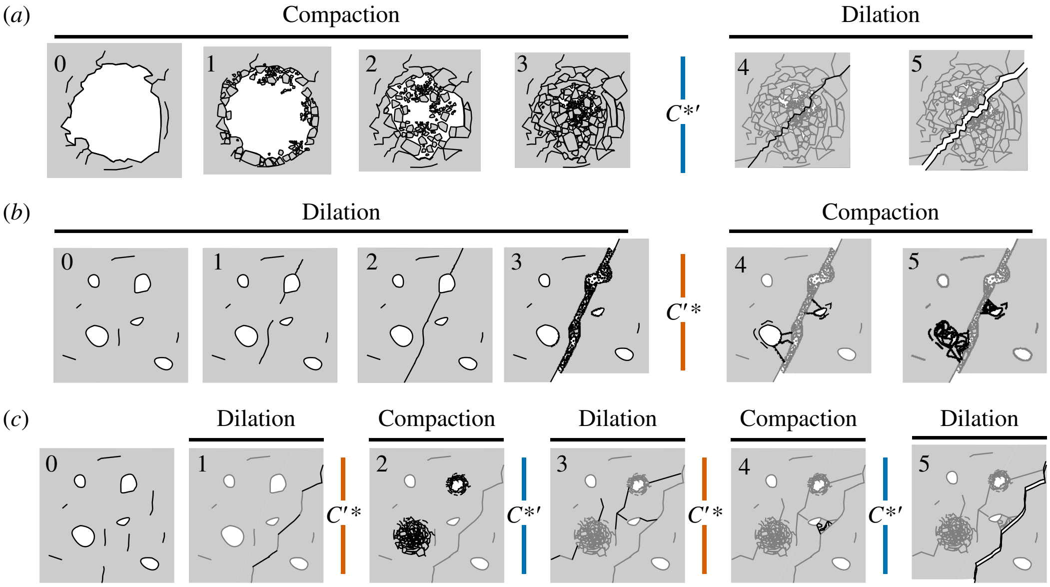

Figure 6. Micromechanical deformation mechanisms. (*a*) Deformation initially characterized by cataclastic pore collapse. During the 'compaction' sequence (0–3), a porous sample (porosity shown in white) is subject to loading. Stress concentration drives cataclasis and pore collapse. Beyond the $C^{*\prime}$ threshold, the primary micromechanisms are the generation, growth and coalescence of fractures (4–5), driving sample dilation. (*b*) Deformation initially characterized by dilatant fracturing. In the 'dilation' sequence (0–3), slight porosity increase is driven by generation (0) and growth (1) of disconnected fractures. As these fractures link up (2, macroscopic failure), a through-running failure plane is created. Sliding on the fault plane leads to evolution of the fault core (3). In this scenario, the sample then undergoes the critical transition $C^{\prime *}$, manifest in the progressive collapse of pores proximal to the fault zone (4–5). (*c*) Deformation initially characterized by dilation, before transitioning between dilation- (1, 3 and 5) and compaction-dominant (2, 4) mechanisms. In this scenario, the sample alternately meets $C^{*\prime}$ and $C^{\prime *}$.

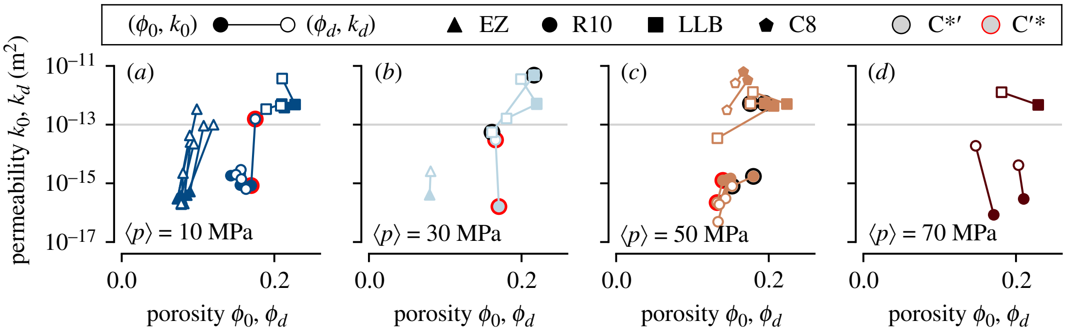

Figure 7. Pre- and post-deformation porosity and permeability shown in solid and open symbols, respectively, for new and compiled andesites. Samples which have undergone $C^{\prime *}$ or $C^{*\prime}$ are highlighted by light red or black circles, respectively. (*a*) Samples deformed at $\langle p \rangle = 10$ MPa. (*b*) Samples deformed at $\langle p \rangle = 30$ MPa. (*c*) Samples deformed at $\langle p \rangle = 50$ MPa. (*d*) Samples deformed at $\langle p \rangle = 70$ MPa. Colours correspond to effective pressure, as in previous figures.

localization (see also [67]). Microstructural evidence indicates that at intermediate sample porosities, compaction bands in volcanic rock can be oriented at oblique angles to the sample axis, rather than perpendicular as observed in other materials [67]. This is proposed to be dependent on sample heterogeneity [17]: pore size shape and distribution in these andesites is complex and variable, which strongly influences their physical and mechanical properties [44]. Moreover, the non-contiguous and diffuse nature of compaction bands in volcanic rock is in contrast to the discrete features sometimes observed in sedimentary rocks [68]. Interestingly, the compilation reveals that post-failure transition from compaction to dilation ($C^{*\prime}$) does little by way of increasing sample permeability (see samples highlighted in black in figure 7*b*,*c*). This is presumably due to the large amounts of strain required to achieve this transition (figure 3*b*), which results in substantial comminution of groundmass (figure 3*c*). The macroscopic fracture zone imposed at $C^{*\prime}$ is generally not oriented favourably to fluid flow ($\theta \sim \pi/2$; figure 3*d*). Nevertheless, permeability reduction in samples having undergone $C^{*\prime}$ is not as pronounced as in samples that were unloaded before this critical stress state was reached, highlighting the contribution of dilatant shear fracture to the effective sample permeability.

At lower effective pressure ($\langle p \rangle = 10$ MPa, figure 7*a*), changes to the porosity and permeability of the R10 andesite samples tend to be subtle. We infer that the highly irregular pore shapes and high crystal cargo [38] impedes the formation of a geometrically simple fracture; rather, macroscopic failure is manifest as a tortuous network of interconnected pores. The exception is the sample that has achieved the critical stress state C'^* (see figure 4): although there is only slight net dilation, permeability increases by approximately two orders of magnitude (highlighted in red on figure 7*a*). This is echoed in figure 7*b* for a sample deformed at $\langle p \rangle = 30$ MPa (highlighted in red): in this case the sample porosity has decreased, but permeability has been enhanced by two orders of magnitude, again having surpassed C'^*. Seemingly, this complex post-failure behaviour, which is (to an extent) self-limiting in terms of net porosity change (figure 5) is a mechanism for the generation of highly efficient fluid flow pathways. As shown in figure 4*c,d*, fluid flow paths may be generated which are oriented $\theta \sim \pi/4$ (approx. 45°) relative to the sample axis and direction of fluid flow.

Much of the variability in the effect of deformation on permeability can be understood by considering the post-deformation samples as a simplified two-dimensional layered medium. A sample of dimensions $L \times \sum_i^n w_i$, where L is length and w_i corresponds to the width of each layer i, can be characterized by its arithmetic and harmonic mean permeabilities $\langle k_x \rangle = (\sum_{i=1}^n w_i k_i)/L$ and $\langle k_z \rangle = L/(\sum_{i=1}^n w_i/k_i)$, respectively [69]. Layer permeabilities are described by k_i. Assuming the sample comprises a host medium of permeability k_0, containing a planar feature ('inclusion') of permeability k_1 (which may be higher or lower than k_0), we can determine both the effect on equivalent permeability $\langle k \rangle$ of varying k_1 and the angle θ of the inclusion with respect to fluid flow via

$$\langle k \rangle = \langle k_z \rangle \sin^2(\theta) + \langle k_x \rangle \cos^2(\theta)\,. \tag{4.1}$$

We visualize equation 4.1 in figure 8, assuming a two-layer medium of dimensions $L \times (w_0 + w_1)$. Values of 40, 15 and 5 mm are imposed for L, w_0 and w_1, respectively, and we use a permeability value for the layer w_0 of $k_0 = 10^{-15}$ m^2. Adopting a range of k_1 from 10^{-18} to 10^{-12} m^2 for the layer (inclusion) w_1 allows us to calculate k_x and k_z, and in turn equivalent permeability $\langle k \rangle$ after equation 4.1. In figure 8, the values of $\langle k \rangle$ as a function of inclusion angle are shown by the coloured lines. From equation 4.1, it follows that if $k_1 \gg k_0$ (i.e. considering a through-running macroscopic fracture), then equivalent permeability will be substantially augmented parallel to the orientation of the inclusion (low θ; see point 1 on figure 8). At $k_1 \ll k_0$ (e.g. considering a dense compaction band), permeability will be greatly diminished perpendicular to the orientation of the inclusion (point 2 on figure 8). At $k_1 \gtrsim k_0$ or $k_1 \lesssim k_0$, changes to equivalent permeability will be slight. Irrespective of the magnitude of $|k_0 - k_1|$, any increase or decrease in $\langle k \rangle$ is strongly dependent on the orientation of the inclusion [69]: a highly permeable fracture oriented perpendicularly to fluid flow ($\theta = \pi/2$) or a low-permeability compaction band oriented parallel to fluid flow ($\theta = 0$) will not deviate $\langle k \rangle$ far from k_0 (i.e. 3 and 4 on figure 8). In our experiments, post-failure samples fall on a spectrum from $k_1 \gg k_0, \theta = 0$ to $k_1 \ll k_0, \theta = \pi/2$, primarily as a function of increasing effective pressure $\langle p \rangle$. From our microstructural data (see also [17]), we posit that compaction localization features in these andesites can rarely be approximated as being oriented at $\pi/2$ with respect to the sample axis (rather, they may be closer to $\pi/3$). Interpreting figure 8 in this context yields the insight that absolute changes in permeability as a function of initial localized failure in porous volcanic rocks is likely to always be greater in the brittle field than the ductile field. Investigating the role of inter-sample heterogeneity, quantifying relevant flaw length scales and their spatial distributions, and in particular the upscaling of these observations beyond the centimetric scale to examine the effects of mechanical deformation on fluid flow are key avenues for future research. Deformation of synthetic or numerical samples [64,70,71], syn-deformation imaging [72–74] and the use of equivalent medium permeability models [69] each hold promise for shedding light on these complexities.

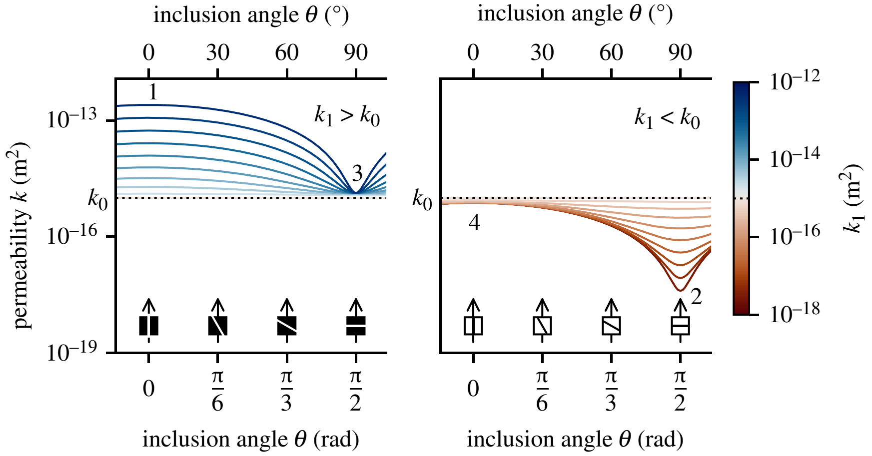

Figure 8. The effect of inclusion angle on equivalent permeability $\langle k \rangle$. Following equation 4.1, $\langle k \rangle$ is calculated for a range of values of k_1 and inclusion angle with respect to the direction of fluid flow (θ), while all other variables are kept constant (host permeability k_0 = 10–15 m^2 (dotted line), sample length L = 40 mm; inclusion layer width w_1 = 5 mm; host layer width $w_0 = 20 - w_1$ mm). $\langle k \rangle$ is shown by the coloured lines, corresponding to k_1. Panels are separated according to whether $k_1 > k_0$ or vice versa. Points 1–4 are mentioned in the text.

5. Implications of the mechanical limit

Our results point to functional limits to both compaction and dilation in natural geological systems. Moreover, we reveal the importance of considering post-failure deformation behaviour, which can significantly modify fluid flow. The samples in this study for which we demonstrate the most complex post-failure deformation contained an initial porosity of approximately 0.16. Compilations of edifice-forming pyroclasts [10,42,43,75] often reveal modal porosities in the range $0.1 < \phi < 0.2$; in line with estimates of edifice porosity from gravimetric inversion [76]. Thus, the results presented here are highly relevant to materials that comprise a volumetrically important proportion of a volcanic edifice. Moreover, samples were deformed herein at effective pressures ranging from 10 to 70 MPa. Lithostatic pressure at depth $p(z)$ is a function of atmospheric (datum) pressure p_0, surface gravitational acceleration g and bulk rock density $\rho(z)$; the relation $p(z) = p_0 + g\int_0^z \rho(z)dz$ indicates that the imposed values of $\langle p \rangle$ represent depths from approximately 400 to 3000 m (ρ = 2320 kg m^{-3}), relevant to shallow crustal processes. This is especially pertinent considering the high stresses and strain associated with magma migration-induced uplift, the ascent and extrusion of lava and related deformation processes.

Deformation of volcanic edifices, including non-magmagenic deformation, is common [77]. Indeed, in a study that systematically monitored 198 volcanoes over 3 years [78], there were more ‘false positives’ than ‘true positives’, which is to say that the incidence of volcanoes remaining quiescent following measurable deformation was higher than volcanoes which erupted after deformation, attributed in part to complexity arising from local stress fields. At many volcanoes, ground deformation changes—detected using global navigation satellite systems (GNSS) or interferometric synthetic aperture radar (InSAR), for example—exhibit variations in rate and/or direction over relatively short timescales (e.g. days or years) [79–81]. A mechanical limit for dilatant and compactive processes in a volcanic edifice, as we describe herein, provides an explanation for alternating surface deformation observed in GNSS or InSAR data that may be seemingly uncorrelated with magmatic activity (figure 9).

Inversion modelling, which typically requires surface displacement data as an input, has indicated that the strength and volumetric response of edifice rock to loading influences the dynamics of magmatic processes. For example, edifice-scale modelling of displacement at Piton de la Fournaise (La Réunion) necessitated a maximum stress accumulation value in the upper edifice, with the authors proposing that nonlinear behaviour and stress periodicity are promoted by the existence of this critical threshold [82]. In turn, this explains complex distal magma migration and allows the volcanic edifice to modulate magma transfer from depth—a so-called ‘valve effect’ controlled by the mechanical evolution of the edifice [82]. Our experimental data support such a mechanism at volcanoes more generally, such that micro- and meso-scale mechanical limits to volumetric change are echoed at the scale of the volcanic superstructure

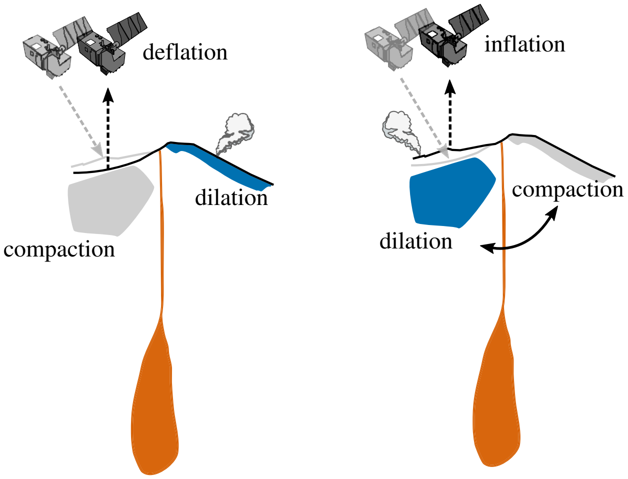

Figure 9. Illustration of the effects of failure mode transitions on volcanic outgassing and observed surface deformation. In the first instance (left panel), a zone of the shallow volcanic edifice is undergoing dilatant deformation, allowing fumarolic outgassing from one flank. A zone of subsurface compaction is manifest as edifice deflation as inferred from ground displacement measurements. Switches in failure mode (centre panel) lead to a reversal in the observed deformation signal and activation of a different fumarole area. In the right panel, a further compaction–dilation/dilation–compaction switch means that the displacement observations revert to their initial state. In this scenario, outgassing is now distributed across both flanks, as permeable fracture networks have been developed and activated in both locations. Circulation of hydrothermal fluids has been promoted, allowing alteration to occur.

(cf. kinematic volcano-tectonic coupling [83] or co- and post-seismic reversals in compressional and extensional quadrants at the field scale [84,85]). Notably, a further study was able to effectively model surface displacements at Piton de la Fournaise by accounting for an 'incremental damage' factor [86], underlining the importance of accounting for ongoing edifice deformation when modelling magma migration based on surface displacement data.

Comparable self-regulating mechanisms have also been proposed to govern near-surface gas loss in volcanic systems [87,88], whereby the time-dependent outgassing capacity of tuffisite networks is reflected in localized fumarole activity. In a similar vein, we suggest that repeated transitions in deformation style throughout the edifice could lead to transient activation and deactivation of discrete outgassing fields (figure 9). A corollary of this is that hydrothermal circulation in the subsurface may be periodically enhanced, promoting alteration [89], mass transfer [1,3] and epithermal ore formation [90] (figure 9). Alteration can in turn be associated with volcanic hazards [91–93]. Volcano-drilling projects have shown that the upper conduit and shallow edifice of silicic to intermediate volcanoes is often intensely damaged. For example, drill cores of Unzendake [29] and Nigorikawa Caldera [30] preserve polymict volcanic breccia rather than intact pristine lava, suggestive of a complex stress–strain history and potentially indicative of multiple overprinting of brittle and ductile deformation mechanisms. The low permeability of exhumed Unzendake drill cores (of order 10^{-19}–10^{-17} m^2 [94]) belies the fact that they must have allowed abundant hydrothermal circulation in their history [95,96], resulting in extensive alteration [97]. Our experimental results emphasize the complex coupling between mechanical deformation and fluid flow in the shallow crust.

6. Conclusions

When subject to applied differential stress, rocks can fail in a dilatant (brittle) or compactant (ductile) manner. However, when deformation continues beyond the initial failure threshold—as may occur in natural crustal settings—the dominant deformation behaviour (dilatant or compactant) may switch. In order to investigate the effect of complex post-failure deformation on the physical rock properties, we conduct a series of triaxial deformation experiments on samples of porous andesite from Ruapehu volcano, Aotearoa New Zealand. This material was selected because its porosity range (approx. 0.14–0.20) is typical of modal porosities of edifice-forming rocks, and it straddles the transition between positive and negative volumetric responses to compression when deformed under effective pressures relevant to the shallow crust (i.e. the inelastic compaction factor $\delta\phi_i\epsilon_i^{-1}$ tends towards zero under differential stress).

As well as demonstrating a post-failure switch from compactant to dilatant behaviour (a phenomenon known as $C^{*\prime}$), we describe for the first time a critical stress state whereat a switch from dilatant to compactant behaviour is observed. We refer to this as $C^{\prime *}$, and demonstrate its occurrence both through new deformation experiments and reappraisal of published experimental data. Critically, samples that achieved this stress state, under volcanically relevant deformation and pressure conditions, exhibited substantial increases in permeability. This is in contrast to samples that undergo $C^{*\prime}$, where any dilatancy-induced enhancement in permeability is effectively masked by the global decrease in sample porosity—a consequence of the high strains generally associated with achieving this transition. Additionally, we show that repeated transitions between dilatant and compactant behaviour are possible. We infer that this reflects a competition between compactant mechanisms (e.g. distributed cracking, cataclastic pore collapse) and dilatant mechanisms (e.g. fracture generation, coalescence and fault sliding), with the dominant process being governed by localized stress changes. We infer that these behaviours are controlled by effective pressure, porosity and sample microstructural heterogeneity.

We emphasize that complex post-failure deformation processes could have important ramifications for the edifice-scale deformation and evolution of gas pressure at shallow depths in volcanic systems—a critical determinant of explosive volcanic activity—as well as influencing thermal and solute transport in the shallow crust. In addition to influencing volcanic hazard, these parameters govern the distribution and abundance of commercially and industrially relevant minerals and metals in porphyry ore deposits, the long-term viability of carbon capture and storage reservoirs and nuclear waste storage in the crust, and the stimulation and productivity of geothermal reservoirs—all of which are key to tackling societal problems in the foreseeable future.

Ethics. This work did not require ethical approval from a human subject or animal welfare committee.

Data accessibility. All new data and the Python code used for analysis and plotting are provided in the GitHub repository https://github.com/jifarquharson/failure-mode-switching, archived via Zenodo at https://doi.org/10.5281/zenodo.1323692 [98].

Supplementary material is available online [99].

Declaration of AI use. We have not used AI-assisted technologies in creating this article.

Authors' contributions. J.I.F.: conceptualization, data curation, formal analysis, investigation, visualization, writing—original draft, writing—review and editing; M.J.H.: conceptualization, funding acquisition, methodology, supervision, writing—review and editing; L.C.: conceptualization, writing—review and editing; P.B.: conceptualization, funding acquisition, methodology, supervision, writing—review and editing.

All authors gave final approval for publication and agreed to be held accountable for the work performed therein.

Conflict of interest declaration. We declare we have no competing interests.

Funding. J.I.F. acknowledges the Initiative d'Excellence (IDEX) framework of the French State, which supported his PhD studies, and start-up funds from Niigata University (543142). M.J.H. acknowledges support from the Institut Universitaire de France (IUF), and was also supported by European Research Council Synergy Grant (ERC-ROTTnROCK-101118491).

Acknowledgements. Gilles Morvan is thanked for his assistance using the scanning electron microscopy, and Bertrand Renaudie is thanked for sample preparation at Université de Strasbourg. We would like to acknowledge Harry Keys and Blake McDavitt at the Department of Conservation New Zealand for their assistance with permitting and access, and we would like to acknowledge the people of Ngāti Tūwharetoa and Ngāti Rangi for their support of work on Mount Ruapehu, which has great cultural significance. We thank Ben Kennedy for facilitating fieldwork in Aotearoa New Zealand. Martha Eppes and Agata Poganj are thanked for helpful discussions. Fabio Crameri is acknowledged for providing open source perceptually uniform colourmaps (Crameri (2018). Scientific colour maps. Zenodo. https://doi.org/10.5281/zenodo.1243862) [100]. We would additionally like to thank the editors, alongside Anthony Lamur and two anonymous referees, whose insightful comments helped improve this manuscript.

References

1. Ingebritsen SE, Gleeson T. 2015 Crustal permeability: introduction to the special issue. *Geofluids* **15**, 1–10. (doi:10.1111/gfl.12118)
2. Manga M, Beresnev I, Brodsky EE, Elkhoury JE, Elsworth D, Ingebritsen SE, Mays DC, Wang CY. 2012 Changes in permeability caused by transient stresses: field observations, experiments, and mechanisms. *Rev. Geophys.* **50**, RG2004. (doi:10.1029/2011RG000382)
3. Ingebritsen SE, Manning CE. 2010 Permeability of the continental crust: dynamic variations inferred from seismicity and metamorphism. *Geofluids* **10**, 193–205. (doi:10.1111/j.1468-8123.2010.00278.x)
4. Farquharson JI, Wadsworth FB, Heap MJ, Baud P. 2017 Time-dependent permeability evolution in compacting volcanic fracture systems and implications for gasoverpressure. *J. Volcanol. Geotherm. Res.* **339**, 81–97. (doi:10.1016/j.jvolgeores.2017.04.025)

5. Cassidy M, Manga M, Cashman K, Bachmann O. 2018 Controls on explosive-effusive volcanic eruption styles. *Nat. Commun*. **9**, 2839. (doi:10.1038/s41467-018-05293-3)
6. Collinson ASD, Neuberg JW. 2012 Gas storage, transport and pressure changes in an evolving permeable volcanic edifice. *J. Volcanol. Geotherm. Res*. **243–244**, 1–13. (doi:10.1016/j.jvolgeores.2012.06.027)
7. Diller K, Clarke AB, Voight B, Neri A. 2006 Mechanisms of conduit plug formation: implications for vulcanian explosions. *Geophys. Res. Lett*. **33**. (doi:10.1029/2006GL027391)
8. Blower J. 2001 Factors controlling permeability-porosity relationships in magma. *Bull. Volcanol.* **63**, 497–504. (doi:10.1007/s004450100172)
9. Eichelberger JC, Carrigan CR, Westrich HR, Price RH. 1986 Non-explosive silicic volcanism. *Nature* **323**, 598–602. (doi:10.1038/323598a0)
10. Farquharson JI, Heap MJ, Varley NR, Baud P, Reuschlé T. 2015 Permeability and porosity relationships of edifice-forming andesites: a combined field and laboratory study. *J. Volcanol. Geotherm. Res*. **297**, 52–68. (doi:10.1016/j.jvolgeores.2015.03.016)
11. Mueller S, Scheu B, Spieler O, Dingwell DB. 2008 Permeability control on magma fragmentation. *Geology* **36**, 399–402. (doi:10.1130/G24605A.1)
12. Rust AC, Cashman KV. 2004 Permeability of vesicular silicic magma: inertial and hysteresis effects. *Earth Planet. Sci. Lett*. **228**, 93–107. (doi:10.1016/j.epsl.2004.09.025)
13. Vasseur J, Wadsworth FB. 2017 Sphere models for pore geometry and fluid permeability in heterogeneous magmas. *Bull. Volcanol*. **79**, 77. (doi:10.1007/s00445-017-1165-1)
14. Ashwell PA, Kendrick JE, Lavallée Y, Kennedy BM, Hess K-U, von Aulock FW, Wadsworth FB, Vasseur J, Dingwell DB. 2015 Permeability of compacting porous lavas. *J. Geophys. Res. Solid Earth* **120**, 1605–1622. (doi:10.1002/2014JB011519)
15. Gonnermann Helge M, Giachetti T, Fliedner C, Nguyen CT, Houghton BF, Crozier JA, Carey RJ. 2017 Permeability during magma expansion and compaction. *J. Geophys. Res. Solid Earth* **122**, 9825–9848. (doi:10.1002/2017JB014783)
16. Heap MJ, Meyer GG, Noël C, Wadsworth FB, Baud P, Violay MES. 2022 The permeability of porous volcanic rock through the brittle-ductile transition. *J. Geophys. Res. Solid Earth* **127**, e2022JB024600. (doi:10.1029/2022JB024600)
17. Heap MJ, Farquharson JI, Baud P, Lavallée Y, Reuschlé T. 2015 Fracture and compaction of andesite in a volcanic edifice. *Bull. Volcanol*. **77**, 55. (doi:10.1007/s00445-015-0938-7)
18. Heap MJ, Farquharson JI, Wadsworth FB, Kolzenburg S, Russell JK. 2015 Timescales for permeability reduction and strength recovery in densifying magma. *Earth Planet. Sci. Lett*. **429**, 223–233. (doi:10.1016/j.epsl.2015.07.053)
19. Kennedy BM *et al*. 2016 Surface tension driven processes densify and retain permeability in magma and lava. *Earth Planet. Sci. Lett*. **433**, 116–124. (doi:10.1016/j.epsl.2015.10.031)
20. Wong T-f, Baud P. 2012 The brittle-ductile transition in porous rock: a review. *J. Struct. Geol*. **44**, 25–53. (doi:10.1016/j.jsg.2012.07.010)
21. Heap MJ, Violay MES. 2021 The mechanical behaviour and failure modes of volcanic rocks: a review. *Bull. Volcanol*. **83**, 33. (doi:10.1007/s00445-021-01447-2)
22. Adelinet M, Fortin J, Schubnel A, Guéguen Y. 2013 Deformation modes in an Icelandic basalt: from brittle failure to localized deformation bands. *J. Volcanol. Geotherm. Res*. **255**, 15–25. (doi:10.1016/j.jvolgeores.2013.01.011)
23. Loaiza S, Fortin J, Schubnel A, Gueguen Y, Vinciguerra S, Moreira M. 2012 Mechanical behavior and localized failure modes in a porous basalt from the azores. *Geophys. Res. Lett*. **39**. (doi:10.1029/2012GL053218)
24. Nara Y, Meredith PG, Yoneda T, Kaneko K. 2011 Influence of macro-fractures and micro-fractures on permeability and elastic wave velocities in basalt at elevated pressure. *Tectonophysics* **503**, 52–59. (doi:10.1016/j.tecto.2010.09.027)
25. Smith R, Sammonds PR, Tuffen H, Meredith PG. 2011 Evolution of the mechanics of the 2004–2008 Mt. St. Helens lava dome with time and temperature. *Earth Planet. Sci. Lett*. **307**, 191–200. (doi:10.1016/j.epsl.2011.04.044)
26. Zhu W, Baud P, Vinciguerra S, Wong T-f. 2011 Micromechanics of brittle faulting and cataclastic flow in Alban Hills tuff. *J. Geophys. Res.Solid Earth* **116**. (doi:10.1029/2010JB008046)
27. Gudmundsson A. 2011 *Rock fractures in geological processes*. Cambridge, UK: Cambridge University Press.
28. Gudmundsson A. 2012 Strengths and strain energies of volcanic edifices: implications for eruptions, collapse calderas, and landslides. *Nat. Hazards Earth Syst. Sci*. **12**, 2241–2258. (doi:10.5194/nhess-12-2241-2012)
29. Goto Y, Nakada S, Kurokawa M, Shimano T, Sugimoto T, Sakuma S, Hoshizumi H, Yoshimoto M, Uto K. 2008 Character and origin of lithofacies in the conduit of unzen volcano, japan. *J. Volcanol. Geotherm. Res*. **175**, 45–59. (doi:10.1016/j.jvolgeores.2008.03.041)
30. 黒墨秀行, 土井宣夫. 2003 濁川カルデラの内部構造 **48**, 259–274. (doi:10.18940/kazan.48.3_259)
31. Fortin J, Stanchits S, Vinciguerra S, Guéguen Y. 2011 Influence of thermal and mechanical cracks on permeability and elastic wave velocities in a basalt from Mt. Etna volcano subjected to elevated pressure. *Tectonophysics* **503**, 60–74. (doi:10.1016/j.tecto.2010.09.028)
32. Farquharson JI, Heap MJ, Baud P. 2016 Strain-induced permeability increase in volcanic rock. *Geophys. Res. Lett.* **43**, 11. (doi:10.1002/2016GL071540)
33. Heap MJ, Baud P, McBeck JA, Renard F, Carbillet L, Hall SA. 2020 Imaging strain localisation in porous andesite using digital volume correlation. *J. Volcanol. Geotherm. Res*. **404**, 107038. (doi:10.1016/j.jvolgeores.2020.107038)
34. Alam AKMB, Niioka M, Fujii Y, Fukuda D, Kodama J. 2014 Effects of confining pressure on the permeability of three rock types under compression. *Int. J. Rock Mech. Min. Sci*. **65**, 49–61. (doi:10.1016/j.ijrmms.2013.11.006)
35. Farquharson JI, Baud P, Heap MJ. 2017 Inelastic compaction and permeability evolution in volcanic rock. *Solid Earth* **8**, 561–581. (doi:10.5194/se-8-561-2017)

36. Vajdova V, Baud P, Wong T. 2004 Compaction, dilatancy, and failure in porous carbonate rocks. *J. Geophys. Res. Solid Earth* **109**. (doi:10.1029/2003JB002508)

37. Schock RN, Heard HC, Stephens DR. 1973 Stress-strain behavior of a granodiorite and two graywackes on compression to 20 kilobars. *J. Geophys. Res.*(*1896-1977*) **78**, 5922–5941. (doi:10.1029/JB078i026p05922)

38. Heap MJ, Kennedy BM. 2016 Exploring the scale-dependent permeability of fractured andesite. *Earth Planet. Sci. Lett.* **447**, 139–150. (doi:10.1016/j.epsl.2016.05.004)

39. Hackett WR, Houghton BF. 1989 A facies model for a quaternary andesitic composite volcano: Ruapehu, New Zealand. *Bull. Volcanol.* **51**, 51–68. (doi:10.1007/BF01086761)

40. Farquharson JI, Heap MJ, Lavallée Y, Varley NR, Baud P. 2016 Evidence for the development of permeability anisotropy in lava domes and volcanic conduits. *J. Volcanol. Geotherm. Res.* **323**, 163–185. (doi:10.1016/j.jvolgeores.2016.05.007)

41. Farquharson JI, Heap MJ, Baud P. 2016 Strain-induced permeability increase in volcanic rock. *Geophys. Res. Lett.* **43**, 11 603–11 610. (doi:10.1002/2016GL071540)

42. Bernard B, Kueppers U, Ortiz H. 2015 Revisiting the statistical analysis of pyroclast density and porosity data. *Solid Earth* **6**, 869–879. (doi:10.5194/se-6-869-2015)

43. Lavallée Y, Heap MJ, Kendrick JE, Kueppers U, Dingwell DB. 2019 The fragility of Volcán de Colima—a material constraint. In *Volcán de Colima: portrait of a persistently hazardous volcano* (eds N Varley, CB Connor, JC Komorowski), pp. 241–266. Berlin, Germany: Springer. (doi:10.1007/978-3-642-25911-1_7)

44. Heap MJ, Lavallée Y, Petrakova L, Baud P, Reuschlé T, Varley NR, Dingwell DB. 2014 Microstructural controls on the physical and mechanical properties of edifice-forming andesites at Volcán de Colima, Mexico. *J. Geophys. Res.* **119**, 2925–2963. (doi:10.1002/2013JB010521)

45. Baud P, Reuschlé T, Ji Y, Cheung CSN, Wong T. 2015 Mechanical compaction and strain localization in Bleurswiller sandstone. *J. Geophys. Res. Solid Earth* **120**, 6501–6522. (doi:10.1002/2015JB012192)

46. Terzaghi K. 1923 Die berechnung der durchlassigkeitsziffer des tones aus dem verlauf der hidrodynamichen spannungserscheinungen akademie der wissenschaften in wien. *Math. Nat. Wiss. Schaftl. Klasse* **132**, 125–138.

47. Biot MA, Willis DG. 1957 The elastic coefficients of the theory of consolidation. *J. Appl. Mech.* **24**, 594–601. (doi:10.1115/1.4011606)

48. Paterson MS, Wong T (eds). 2005 The role of pore fluids. In *Experimental rock deformation — the brittle field,* pp. 147–163. Berlin, Germany: Springer. (doi:10.1007/3-540-26339-X_7)

49. Farquharson JI, Heap MJ, Baud P, Reuschlé T, Varley NR. 2016 Pore pressure embrittlement in a volcanic edifice. *Bull. Volcanol.* **78**, 6. (doi:10.1007/s00445-015-0997-9)

50. Heap MJ, Wadsworth FB. 2016 Closing an open system: pore pressure changes in permeable edifice rock at high strain rates. *J. Volcanol. Geotherm. Res.* **315**, 40–50. (doi:10.1016/j.jvolgeores.2016.02.011)

51. Read MD, Ayling MR, Meredith PG, Murrell SAF. 1995 Microcracking during triaxial deformation of porous rocks monitored by changes in rock physical properties, II. Pore volumometry and acoustic emission measurements on water-saturated rocks. *Tectonophysics* **245**, 223–235. (doi:10.1016/0040-1951(94)00236-3)

52. Baud P, Wong T, Zhu W. 2014 Effects of porosity and crack density on the compressive strength of rocks. *Int. J. Rock Mech. Min. Sci.* **67**, 202–211. (doi:10.1016/j.ijrmms.2013.08.031)

53. Baud P, Vajdova V, Wong T. 2006 Shear-enhanced compaction and strain localization: inelastic deformation and constitutive modeling of four porous sandstones. *J. Geophys. Res. Solid Earth* **111**. (doi:10.1029/2005JB004101)

54. Wong T, David C, Zhu W. 1997 The transition from brittle faulting to cataclastic flow in porous sandstones: mechanical deformation. *J. Geophys. Res. Solid Earth* **102**, 3009–3025. (doi:10.1029/96JB03281)

55. Tierz P, Loughlin SC, Calder ES. 2019 VOLCANS: an objective, structured and reproducible method for identifying sets of analogue volcanoes. *Bull. Volcanol.* **81**, 76. (doi:10.1007/s00445-019-1336-3)

56. Tierz P, Christodoulou V, Stevenson J, Loughlin S. 2021 PyVOLCANS: A python package to flexibly explore similarities and differences between volcanic systems. *JOSS* **6**, 3649. (doi:10.21105/joss.03649)

57. Baud P, Hall S, Heap MJ, Ji Y, Wong T. 2021 The brittle-ductile transition in porous limestone: failure mode, constitutive modeling of inelastic deformation and strain localization. *J. Geophys. Res. Solid Earth* **126**, e2020JB021602. (doi:10.1029/2020JB021602)

58. Baud P, Zhu W, Wong T. 2000 Failure mode and weakening effect of water on sandstone. *J. Geophys. Res. Solid Earth* **105**, 16371–16389. (doi:10.1029/2000JB900087)

59. Regnet JB, David C, Fortin J, Robion P, Makhloufi Y, Collin PY. 2015 Influence of microporosity distribution on the mechanical behavior of oolithic carbonate rocks. *Geom. Mech. Energy Environ.* **3**, 11–23. (doi:10.1016/j.gete.2015.07.002)

60. Meyer GG, Violay M. 2023 Bounding the localized to ductile transition in porous rocks: implications for geo-reservoirs. *Geophys. J. Int.* **235**, 2361–2371. (doi:10.1093/gji/ggad377)

61. Heap MJ, Russell JK, Kennedy LA. 2016 Mechanical behaviour of dacite from Mount St. Helens (USA): a link between porosity and lava dome extrusion mechanism (dome or spine)? *J. Volcanol. Geotherm. Res.* **328**, 159–177. (doi:10.1016/j.jvolgeores.2016.10.015)

62. Heap MJ, Baud P, Meredith PG, Bell AF, Main IG. 2009 Time-dependent brittle creep in darley dale sandstone. *J. Geophys. Res. Solid Earth* **114**, B07203. (doi:10.1029/2008JB006212)

63. Engelder JT. 1974 Cataclasis and the generation of fault gouge. *Geol. Soc. Am. Bull.* **85**, 1515–1522. (doi:10.1130/0016-7606(1974)85<1515:CATGOF>2.0.CO;2)

64. Carbillet L, Heap MJ, Baud P, Wadsworth FB, Reuschlé T. 2021 Mechanical compaction of crustal analogs made of sintered glass beads: the influence of porosity and grain size. *J. Geophys. Res.Solid Earth* **126**, e2020JB021321. (doi:10.1029/2020JB021321)
65. Klein E, Baud P, Reuschlé T, Wong T. 2001 Mechanical behaviour and failure mode of Bentheim sandstone under triaxial compression. *Phys. Chem. Earth. A Solid Earth. Geod.* **26**, 21–25. (doi:10.1016/S1464-1895(01)00017-5)
66. Sari M, Sarout J, Poulet T, Dautriat J, Veveakis M. 2022 The brittle–ductile transition and the formation of compaction bands in the Savonnières limestone: impact of the stress and pore fluid. *Rock Mech. Rock Eng*. **55**, 6541–6553. (doi:10.1007/s00603-022-02963-z)
67. Baud P, Meredith P, Townend E. 2012 Permeability evolution during triaxial compaction of an anisotropic porous sandstone. *J. Geophys. Res*. **117**, 2012JB009176. (doi:10.1029/2012JB009176)
68. Louis L, Wong T, Baud P, Tembe S. 2006 Imaging strain localization by X-ray computed tomography: discrete compaction bands in Diemelstadt sandstone. *J. Struct. Geol.* **28**, 762–775. (doi:10.1016/j.jsg.2006.02.006)
69. Farquharson JI, Wadsworth FB. 2018 Upscaling permeability in anisotropic volcanic systems. *J. Volcanol. Geotherm. Res*. **364**, 35–47. (doi:10.1016/j.jvolgeores.2018.09.002)
70. Heap MJ, Wadsworth FB, Xu T, Chen C, Tang C. 2016 The strength of heterogeneous volcanic rocks: a 2D approximation. *J. Volcanol. Geotherm. Res.* **319**, 1–11. (doi:10.1016/j.jvolgeores.2016.03.013)
71. Carbillet L, Wadsworth FB, Heap MJ, Baud P. 2023 Microstructural controls on the uniaxial compressive strength of porous rocks through the granular to non-granular transition. *Geophys. Res. Lett*. **50**, e2023GL104678. (doi:10.1029/2023GL104678)
72. Heap MJ, Harnett CE, Nazarbayov T, Heng Z, Baud P, Xu T, Rosas-Carbajal M, Komorowski JC. 2023 The influence of heterogeneity on the strength of volcanic rocks and the stability of lava domes. *Bull. Volcanol*. **85**, 49. (doi:10.1007/s00445-023-01669-6)
73. Huang L, Baud P, Cordonnier B, Renard F, Liu L, Wong T. 2019 Synchrotron X-ray imaging in 4D: multiscale failure and compaction localization in triaxially compressed porous limestone. *Earth Planet. Sci. Lett.* **528**, 115831. (doi:10.1016/j.epsl.2019.115831)
74. Meng F, Huang L, Baud P, Wong T. 2023 Strain localization in 4D imaged by X-ray computed tomography and digital volume correlation: discrete compaction bands in Leitha limestone. *J. Mech. Phys. Solids* **171**, 105160. (doi:10.1016/j.jmps.2022.105160)
75. Mueller S, Scheu B, Kueppers U, Spieler O, Richard D, Dingwell DB. 2011 The porosity of pyroclasts as an indicator of volcanic explosivity. *J. Volcanol. Geotherm. Res*. **203**, 168–174. (doi:10.1016/j.jvolgeores.2011.04.006)
76. Tiede C, Camacho AG, Gerstenecker C, Fernández J, Suyanto I. 2005 Modeling the density at Merapi volcano area, Indonesia, via the inverse gravimetric problem. *Geochem. Geophys. Geosyst*. **6**. (doi:10.1029/2005GC000986)
77. Biggs J, Wright TJ. 2020 How satellite InSAR has grown from opportunistic science to routine monitoring over the last decade. *Nat. Commun*. **11**, 3863. (doi:10.1038/s41467-020-17587-6)
78. Biggs J, Ebmeier SK, Aspinall WP, Lu Z, Pritchard ME, Sparks RSJ, Mather TA. 2014 Global link between deformation and volcanic eruption quantified by satellite imagery. *Nat. Commun*. **5**, 3471. (doi:10.1038/ncomms4471)
79. Pritchard ME, Mather TA, McNutt SR, Delgado FJ, Reath K. 2019 Thoughts on the criteria to determine the origin of volcanic unrest as magmatic or non-magmatic. *Phil. Trans. R. Soc. A*. **377**, 20180008. (doi:10.1098/rsta.2018.0008)
80. Morales Rivera AM, Amelung F, Mothes P. 2016 Volcano deformation survey over the Northern and Central Andes with ALOS InSAR time series. *Geochem. Geophys. Geosyst*. **17**, 2869–2883. (doi:10.1002/2016GC006393)
81. Wicks CW, Thatcher W, Dzurisin D, Svarc J. 2006 Uplift, thermal unrest and magma intrusion at Yellowstone caldera. *Nature* **440**, 72–75. (doi:10.1038/nature04507)
82. Got JL, Peltier A, Staudacher T, Kowalski P, Boissier P. 2013 Edifice strength and magma transfer modulation at Piton de la Fournaise volcano. *J. Geophys. Res*. **118**, 5040–5057. (doi:10.1002/jgrb.50350)
83. Cembrano J, Lara L. 2009 The link between volcanism and tectonics in the southern volcanic zone of the Chilean Andes: a review. *Tectonophysics* **471**, 96–113. (doi:10.1016/j.tecto.2009.02.038)
84. Jónsson S, Segall P, Pedersen R, Björnsson G. 2003 Post-earthquake ground movements correlated to pore-pressure transients. *Nature* **424**, 179–183. (doi:10.1038/nature01776)
85. Pérez-Estay N, Ruz-Ginouves J, Pérez-Flores P, Sielfeld G, Roquer T, Cembrano J. 2023 Decoding the state of stress and fluid pathways along the Andean Southern Volcanic Zone. *Commun. Earth Environ*. **4**, 1–15. (doi:10.1038/s43247-023-01040-9)
86. Carrier A, Got JL, Peltier A, Ferrazzini V, Staudacher T, Kowalski P, Boissier P. 2015 A damage model for volcanic edifices: implications for edifice strength, magma pressure, and eruptive processes. *J. Geophys. Res*. *Solid Earth* **120**, 567–583. (doi:10.1002/2014JB011485)
87. Kolzenburg S, Ryan AG, Russell JK. 2019 Permeability evolution during non-isothermal compaction in volcanic conduits and tuffisite veins: implications for pressure monitoring of volcanic edifices. *Earth Planet. Sci. Lett*. **527**, 115783. (doi:10.1016/j.epsl.2019.115783)
88. Lavallée Y *et al*. 2022 Transient conduit permeability controlled by a shift between compactant shear and dilatant rupture at Unzen volcano (Japan). *Solid Earth* **13**, 875–900. (doi:10.5194/se-13-875-2022)
89. Salaün A, Villemant B, Gérard M, Komorowski JC, Michel A. 2011 Hydrothermal alteration in andesitic volcanoes: trace element redistribution in active and ancient hydrothermal systems of Guadeloupe (Lesser Antilles). *J. Geochem. Explor*. **111**, 59–83. (doi:10.1016/j.gexplo.2011.06.004)
90. Rowland JV, Simmons SF. 2012 Hydrologic, magmatic, and tectonic controls on hydrothermal flow, Taupo Volcanic Zone, New Zealand: implications for the formation of epithermal vein deposits. *Econ. Geol*. **107**, 427–457. (doi:10.2113/econgeo.107.3.427)
91. Darmawan H *et al*. 2022 Hidden mechanical weaknesses within lava domes provided by buried high-porosity hydrothermal alteration zones. *Sci. Rep*. **12**, 3202. (doi:10.1038/s41598-022-06765-9)
92. Heap MJ *et al*. 2021 Hydrothermal alteration can result in pore pressurization and volcano instability. *Geology* **49**, 1348–1352. (doi:10.1130/G49063.1)

93. Detienne M, Delmelle P. 2016 Impact of hydrothermal alteration on lava dome stability: a numerical modelling approach. *EGU General Assembly Conf. Abstracts* EPSC2016–8747.

94. Watanabe T, Shimizu Y, Noguchi S, Nakada S. 2008 Permeability measurements on rock samples from Unzen Scientific Drilling Project Drill Hole 4 (USDP-4). *J. Volcanol. Geotherm. Res*. **175**, 82–90. (doi:10.1016/j.jvolgeores.2008.03.021)

95. Sakuma S, Kajiwara T, Nakada S, Uto K, Shimizu H. 2008 Drilling and logging results of USDP-4—penetration into the volcanic conduit of Unzen Volcano, Japan. *J. Volcanol. Geotherm. Res*. **175**, 1–12. (doi:10.1016/j.jvolgeores.2008.03.039)

96. Nakada S, Uto K, Sakuma S, Eichelberger JC, Shimizu H. 2005 Scientific results of conduit drilling in the Unzen Scientific Drilling Project (USDP). *Sci. Drill.* **1**, 18–22. (doi:10.2204/iodp.sd.3.01.2006)

97. Yilmaz TI *et al*. 2021 Rapid alteration of fractured volcanic conduits beneath Mt Unzen. *Bull. Volcanol*. **83**, 34. (doi:10.1007/s00445-021-01450-7)

98. FarquharsonJ. 2024 Jifarquharson/failure-mode-switching: farquharson-et-al_2024_rsos (v1.0.1). *Zenodo* (doi:10.5281/zenodo.12634612)

99. Farquharson JI, Heap M, Carbillet L, Baud P. 2024 Supplementary material from: Post-failure deformation mode switching in volcanic rock. Figshare. (doi:10.6084/m9.figshare.c.7414276)

100. Crameri F. 2018 Data from: Scientific colour maps. *Zenodo.* (doi:10.5281/zenodo.1243862)